Analysis of stress distributions under lightweight wheeled vehicles

C. Senatore[a,1,*], K. Iagnemma[a,1]

[a]*Laboratory for Manufacturing and Productivity, Massachusetts Institute of Technology, Cambridge, MA 02141, USA.*

Abstract

In recent years, the need for reliable modeling tools for lightweight robotic systems deployed on various terrains has spurred research efforts into development of vehicle terrain interaction (VTI) models. This paper presents an analysis of rigid wheels - dry sand interaction and compares experimental results with predictions from established terramechanics theory. A novel experimental setup, based on sensing elements placed on the wheel surface, allows inference of normal and tangential stress at the wheel-terrain interface. A particle image velocimetry (PIV) analysis is used to study the soil kinematics under the wheel. The analysis of stress profiles shows that stress patterns under lightweight vehicle wheels conform reasonably well to established terramechanics theory developed for heavy vehicles. For the wheel under investigation, the stress distribution had minor variation along wheel width for low slip conditions. The wheel model proposed by Wong and Reece was analyzed in light of the stress and soil kinematics measurements available. It was found that, by appropriately characterizing the model coefficients c_1 and c_2, and understanding the physical meaning of the shear modulus k_x, it is possible to obtain torque, drawbar force, and sinkage predictions within 11% (full scale error) of experimental data.

Keywords: Wheel Model, Shear Strength, Stress Sensor, Granular Particle Image Velocimetry, Terrain Shearing Failure, Wheel Dynamics, Off-Road Vehicle Performance

*Corresponding author

Email addresses: senator@mit.edu (C. Senatore), kdi@mit.edu (K. Iagnemma)

1. Introduction

In recent years, the analysis of lightweight robotic system mobility has raised many questions regarding whether classical terramechanics theory for wheeled vehicles is accurately predictive for reduced scale vehicles [6, 16, 3, 10]. Lacking a standardized classification, in this paper we arbitrarily define lightweight vehicles as having average ground pressure below 20 kPa. Many space rovers and robotic ground vehicles fall within this classification.

Basing his analysis on fundamental concepts of soil mechanics, Bekker [2] introduced a theory to predict mobility of wheeled and tracked vehicles in off-road scenarios. Bekker proposed a set of semi-empirical equations to predict different mobility aspects, such as compaction resistance, traction, sinkage, and driving torque. Bekker himself noted that terramechanics theory "become less accurate for wheels smaller than 20 inches [...] and for wheel loads below about 10 lbs". Carrier [6], while studying the trafficability of lunar micro rovers, concluded that classical Bekker equations lead to an underestimation of small rover tractive performance. Richter et al. [16] investigated the performance of wheels with diameter ranging between 150 mm and 250 mm and vertical loads ranging from 10 N up to 120 N, and concluded that classical Bekker model needs corrections in order to accurately predict performance. Meirion-Griffith and Spenko [10] used small wheels as penetration plates, and noted that Bekker's pressure-sinkage equation 21 is affected by wheel curvature. Griffith and Spenko proposed a modified Bekker pressure-sinkage equation to account for small wheels' curvature.

The theory for off road rigid wheel mobility evaluation developed by Bekker was further refined by Wong and Reece [23, 24]. Wong and Reece did not simply apply correction factors to Bekker equations, but rather expanded the Bekker methodology to calculate wheel performance through the prediction of stress distributions at the wheel-terrain interface. The model proposed by Wong and Reece (here referred to as the WR model) has the merit of deriving all wheel performance metrics (i.e., drawbar force, torque, and sinkage) from the calculated stress distributions at the interface. On the other hand, Bekker's original approach was based on a series of ad-hoc formulations intended to model each single aspect of vehicle mobility independently.

Ishigami et al. [7] showed that a WR-based model could reasonably replicate single wheel experiments (though only positive slip was investigated). However, in [7] it is not discussed how soil parameters were calculated, and therefore it is reasonable to assume that some soil parameters were tuned to match the experimental observations. Ding et al.[3], noting a significant discrepancy between

measured and predicted sinkage, proposed a modified WR model where the sinkage exponent (see APPENDIX A) is modified according to slip. Based on the authors' own experience, tuning of WR model parameters is inevitably required to achieve accurate model predictions across a broad range of loading and slip conditions.

This brief overview of the most significant work on lightweight vehicle mobility modeling shows that previous studies have either proposed modifications of the Bekker-Wong-Reece models (typically by introducing additional parameters) or they have arbitrarily tuned some parameters to improve correlation with experimental data. In either case, the inherent reasons for poor model performance were not investigated.

To overcome these issues, in this paper we describe a detailed analysis of stress distributions under small-sized rigid wheels operating on cohesionless soil in order to understand if, where, and how WR models fail. (Note that the original Bekker model is not discussed). A custom force sensing array located at the wheel-terrain interface is used to measure stresses at the wheel interface. The force sensors are strain gage-based flexural elements with interchangeable interface surfaces that are designed for integration with wheels or other running gear. The sensors allow explicit measurement of normal and shear forces (and, therefore, estimation of normal and shear stresses) at numerous discrete points along the wheel-soil interface. Similar experimental methodologies were employed by Hegedus [4], Sela [17], Onafeko and Reece [15], Krick [9], and Shamay [20]. The key difference is that in [4, 17, 15, 9, 20] the average wheel ground pressure was approximately 100 kPa, while in this paper the wheel average ground pressure is on the order of 10 kPa. (The average ground pressure is evaluated as the nominal wheel load distributed over a flat wheel section spanning 30 degrees). Oida et al. [14] instrumented a flexible tire with a sensor, based on Krick's design [9], and they measured normal, tangential, and lateral stress at the tire-sand interface (however the vertical load and tire dimensions are unknown). Nagatani et al. [13] have used stock button-type force transducers to measure normal stress at wheel-terrain interface. Although the average ground pressure was comparable to what is studied here, the setup proposed in [13] was only able to measure normal load.

Another experimental methodology employed in this work relies on imaging of the wheel-soil interface and the use of particle image velocimetry (PIV) to measure micro-scale terrain displacement. This methodology, although confined to a plane strain case, allows measurement of the soil displacement field under the wheel. Though, this method does not explicitly permit calculation of the

Table 1: Wong and Reece wheel model terrain parameters and coefficients.

Symbol	Units	Description
n	n/a	sinkage exponent
k_c	kN/m^{n+1}	pressure-sinkage coefficient
k_ϕ	kN/m^{n+2}	pressure-sinkage coefficient
c	Pa	cohesion
ϕ	deg	angle of internal friction
k_x	m	shear deformation modulus
c_1, c_2	n/a	coefficients for determining the relative position of maximum radial stress
θ_r	deg	exit angle

velocities of individual soil particles, it does allow estimation of a regularly-spaced velocity field in the soil. While such visualization techniques have been widely employed in the field of experimental fluid mechanics, their application to the study of soils is a relatively new development [21, 11, 12].

Measurements of stress distributions and the soil velocity field are complemented by an in-depth comparison with WR model predictions. The model relies on a set of 6 terrain parameters and 3 wheel-terrain interaction coefficients, presented in Table 1. This work identifies the shear modulus, k_x, and the coefficients for determining the relative position of the maximum radial stress, c_1 and c_2, as the principal factors that often lead to poor performance of WR model predictions.

Here, we have confined our study to wheel operation on dry sand. The sand utilized in this paper has been fully characterized via a series of direct shear tests (ASTM D3080) and penetration tests. Direct shear tests were performed to estimate shearing parameters such as cohesion, c, angle of internal friction, ϕ, and shear modulus k_x. Penetration tests, although not standard tests, were performed to evaluate the "Bekker parameters" n, k_c, and k_ϕ, which are necessary for characterization of the pressure-sinkage behavior of the soil. The key questions that this paper addresses are:

Q1 Are the stress distribution that form under lightweight wheels similar in nature to those that form under heavy weight vehicles?

Q2 Is the WR wheel model capable of accurately modeling lightweight vehicle mobility?

The paper is organized as follows: Experimental Setup presents the terramechanics rig, the custom sensing array, and the PIV setup utilized for this work. Experimental Data Collection and Discussion section is articulated in 6 subsections: first we present an overview of measured stress distributions under the wheel; then we compare the output produced by the custom sensing array with the readings obtained by other sensors installed on the wheel/rig; subsequently we investigate coefficients c_1 and c_2 and how these affect wheel slip-sinkage behavior; we then proceed to analyze PIV data in order to understand soil shear displacement modelling at the wheel-soil interface; next we use this analysis to understand how the shear modulus k_x affects shear stress; finally we present a modified WR model.

2. Experimental Setup

2.1. Single Wheel Test Rig

The Robotic Mobility Group at MIT has designed and fabricated a multipurpose terramechanics rig based on the standard design described by Iagnemma [5]. The testbed is pictured in Figure 1(a) and it is composed of a Lexan soil bin surrounded by an aluminum frame where all the moving parts, actuators and sensors are attached. A carriage slides on two low-friction rails to allow longitudinal translation while the wheel or track, attached to the carriage, is able to rotate at a desired angular velocity. The wheel mount is also able to freely translate in the vertical direction. This typical setup allows control of slip and vertical load by modifying the translational velocity of the carriage, angular velocity of the wheel, and applied load. Horizontal carriage displacement is controlled through a toothed belt actuated by a 90 W Maxon DC motor, while the wheel is directly driven by a 200 W Maxon DC motor. The motors are controlled through two identical Maxon ADS 50/10 4-Q-DC servoamplifiers. The carriage horizontal displacement is monitored with a Micro Epsilon WPS-1250-MK46 draw wire encoder while wheel vertical displacement (i.e., sinkage) is measured with a Turck A50 draw wire encoder.

A 6-axis force torque ATI Omega 85 transducer is mounted between the wheel mount and the carriage in order to measure vertical load and traction generated by the wheel. Finally, a flange-to-flange reaction torque sensor from Futek (TFF500) is used to measure driving torque applied to the wheel. Control and measurement signals are handled by a NI PCIe-6363 card through Labview software. The rig is capable of approximately 1 meter of horizontal displacement at a maximum velocity of approximately 120 mm/s with a maximal wheel angular velocity of approximately 40 deg/s. The bin width is 0.6 meters while the soil

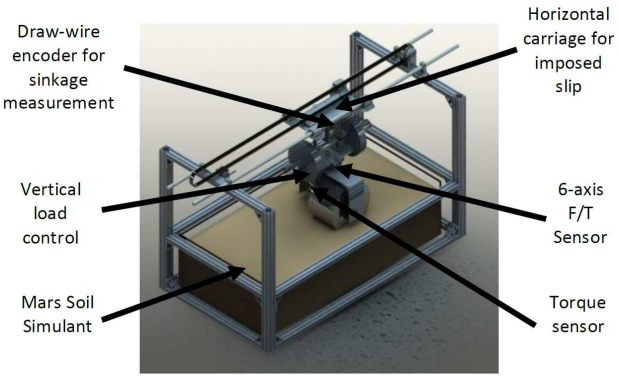

(a)

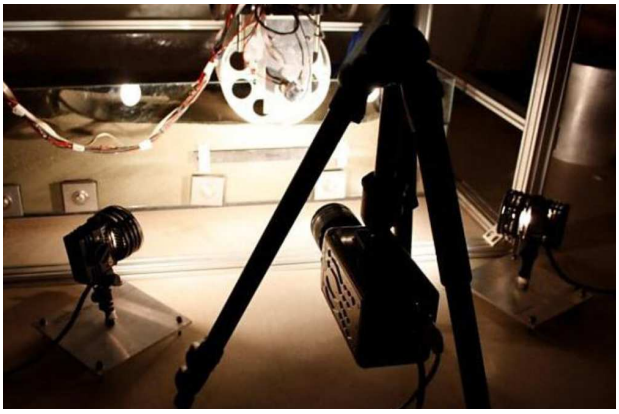

(b)

Figure 1: (a) The terramechanics rig at MIT (b) equipped with imager and lighting for PIV analysis.

depth is 0.16 meters. Considering the wheel sizes and vertical loads under study, these physical dimensions are sufficient for eliminating boundary effects.

Moreover, the same testbed, with some adaptations, can be used to perform soil penetration tests. For the experiments described in this paper, the Mojave Martian Simulant (MMS) was employed as a test medium [1]. MMS is a mixture of finely crushed and sorted granular basalt intended to mimic, both at chemical and mechanical levels, the Mars soil characteristics. MMS particle size distribution spans from micron to millimeter scale, with 80% of particles above the 10 micron threshold. Soil properties were measured through a series of plate penetration tests and direct shear tests: nominal MMS soil parameters are presented in Table 2. It should be noted that the shear modulus is very small. Typical literature values range between 0.01 and 0.03 m, however, as was presented in [18],

Table 2: Mojave Martian Simulant (MMS) properties measured through a series of plate penetration tests and direct shear tests. It should be noted that the shear modulus is very small. Typical literature values range between 0.01 and 0.03 m, however, as was presented in [18], correct calculation of shear modulus leads to a significantly smaller value of k_x.

Symbol	Value	Units
n	1.4	n/a
k_c	846	kN/m^{n+1}
k_ϕ	6708	kN/m^{n+2}
c	600	Pa
ϕ	35	deg
k_x	0.0006	m

correct calculation of shear modulus leads to a significantly smaller value of k_x.

2.2. Force Transducers

The sensing elements used to measure forces at the wheel-terrain interface are custom-made flexural devices equipped with strain gages; similar designs have been used in [9, 20]. Each sensor is composed of an L-shaped beam equipped with 350 ohm strain gages placed on the two arms of the fixture as shown in Figure 2(a) . Two pairs of strain gages are connected to each surface of the beam element in a full-bridge configuration, allowing maximal bending response and naturally rejecting axial loading. Considering the symmetry of the problem, only half of the wheel width was equipped with sensors, as shown in Figure 2(b).

The sensor was designed to maximize strain at points g_1 and g_2 while keeping the sensor head displacements below 0.2 mm. Considering 0-100 kPa as a pressure range, the sensor was designed to withstand loads up to 18 N, with a sensitivity of approximately 0.01 N. If F_1 and F_2 are the tangential and normal loads acting at the tip of the sensor, g_1 and g_2 are the readings from the strain gages, d_1 and d_2 are the distances of the gages from the tip, and ε is the normal load offset; the following system of linear equations holds:

$$g_1 = F_1 d_1 + F_2 \varepsilon \tag{1}$$

$$g_2 = F_1 d_1 + F_2 d_2 + F_2 \varepsilon \tag{2}$$

Solving for F_1 and F_2:

$$F_2 = \frac{g_2 - g_1}{d_2} \tag{3}$$

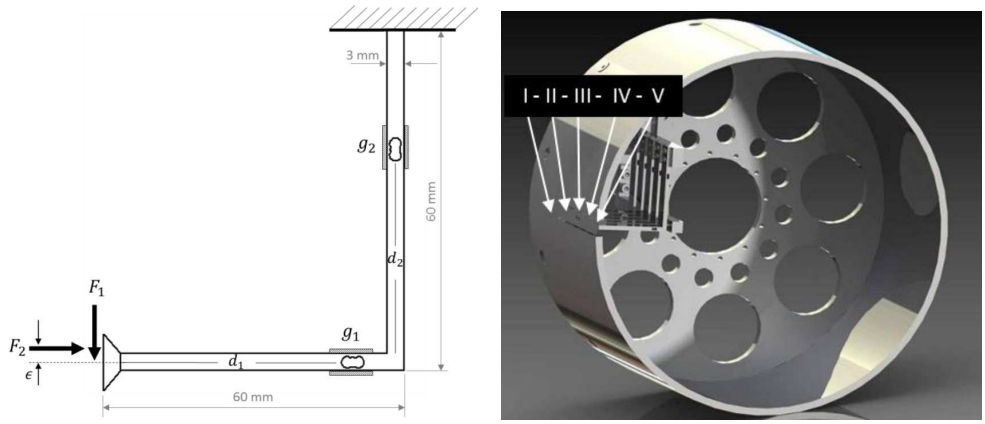

(a) (b)

Figure 2: (a) Schematic of the custom force sensor for interfacial stress measurement. Sensor body is 12 mm wide while sensor head has an area of 10 mm x 18 mm. (b) Five sensors are distributed from the wheel median axis to the wheel edge. Sensors are rigidly connected to the wheel hub.

$$F_1 = \frac{g_1}{d_1} - \frac{F_2 \varepsilon}{d_1} \tag{4}$$

Therefore, the tangential load F_1 is not independent of F_2 in the presence of an asymmetric pressure distribution over the sensor's head. (If the pressure distribution is uniform, the offset ε would be zero). Assuming that the normal pressure distribution is linear along the sensor head, the offset ε is equal to $\sim$1.6 mm, and therefore F_1 can be corrected once F_2 is calculated. It should be noted that the offset error is minimized by design, because $\varepsilon/d_1 \sim= 0.03$, while the normal stress distribution is non-uniform only in the proximity of the terrain entry and exit regions (where, on the other hand, normal stress is small in absolute value).

Calibration of the flexure elements was performed by loading the sensors in the tangential and normal direction with test weights of 100 g, 200 g, and 500 g. The results (presented in Table 3) show that the transducer error is always below 2%. Calibration factors were obtained by minimizing the least square error among all the calibration tests performed. When assembled on the wheel, the sensing array showed to be extremely sensitive to transducer positioning: minimal misalignment of transducer heads would produce skewed readings due to the uneven contact geometry. This issue was controlled by repeatedly testing the wheel on a hard, flat surface, and adjusting individual sensor positions while verifying a uniform output across all sensors.

Table 3: Force sensing array calibration. Accuracy is within 2%.

F_1	Sensor I		Sensor II		Sensor III		Sensor IV		Sensor V	
Nominal Load [g]	Reading [g]	Error [%]	Reading [g]	Error [%]	Reading [g]	Error [%]	Reading [g]	Error [%]	Reading [g]	Error [%]
100	100.1	0.14	101.0	0.99	99.7	-0.29	100.1	0.09	100.1	0.14
200	201.7	0.84	200.8	0.42	200.6	0.29	200.2	0.12	196.8	-1.58
500	498.9	-0.22	498.9	-0.21	499.7	-0.07	499.5	-0.11	500.7	0.13

F_2	Sensor I		Sensor II		Sensor III		Sensor IV		Sensor V	
Nominal Load [g]	Reading [g]	Error [%]	Reading [g]	Error [%]	Reading [g]	Error [%]	Reading [g]	Error [%]	Reading [g]	Error [%]
100	98.2	-1.76	100.8	0.82	100.0	0.00	98.5	-1.49	101.3	1.28
200	199.1	-0.45	199.9	-0.04	200.6	0.30	199.2	-0.42	201.2	0.62
500	499.5	-0.10	499.8	-0.05	499.8	-0.05	500.4	0.07	500.5	0.10

2.3. Particle Image Velocimetry

For PIV experiments, the Lexan soil bin was fitted with a 0.0254 m thick tempered glass wall while the running gear was operated flush against this surface (see Figure 1(b)). It should be noted that stress measurements and particle image velocimetry experiments were conducted independently (i.e., a wheel with the exact same dimensions, but not equipped with interfacial force transducers, was used for PIV experiments).

Image sets for the PIV measurements were captured with a Phantom 7 high-speed camera. The Phantom 7 is able to record grayscale images at a maximum resolution of 800x600 pixels at a maximum frame rate of 6688 fps. The camera was placed perpendicular to the front glass wall (see Figure 1(b)) at a distance of 0.52 m, while its focal length was set to 77 mm (a zoom lens was used) resulting in an image capture region of approximately 0.15 x 0.11 m. It should be noted that determination of image capture region size is largely dictated by the particular experimental conditions. Here, the image capture region was chosen to conservatively bound the region of soil that would undergo motion when subjected to wheel passage on the soil surface. As noted previously, the MMS particle size distribution spans from the micron level to mm level with 80 % of particles above the 10 micron threshold. For the imager configuration described below, the average particle density resulted in approximately 0.044 pixels per particle.

Since soil-glass friction could not be accurately controlled, it should be noted

that calculated velocities and strain are influenced by soil-glass friction. When setting up a similar experiment, Wong [22] proposed to use a wheel with half the nominal width, and to reduce the normal load to half as well. The rationale was that, assuming negligible frictional drag, the glass becomes a plane of symmetry, and therefore the soil motion is analogous to the motion under the median axis of a full sized wheel.

In this paper, we did not follow this approach for two reasons: vertical load and wheel size do not scale linearly; and even assuming linear scaling this would require wheels of different width for every vertical load to be tested. Therefore, assuming limited soil-glass friction and minor stress non-uniformity along the wheel width [19], the soil motion at the glass interface remains representative of the soil motion under the wheel.

3. Experimental Data Collection and Discussion

Tests were conducted with a smooth aluminium wheel of 0.13 m radius and 0.16 m width. The wheel was coated with a layer of soil in order to ensure an adequate level of friction between the wheel surface and the terrain. This wheel has approximately the same dimension of a NASA Mars exploration rover (MER), a successful lightweight robotic system. Three vertical loads have been investigated, 70 N, 100 N (nominal for MER rovers), and 150 N, while 9 slip levels were selected: -70%, -50%, -30%, -10%, 0%, +10%, +30%, +50%, +70%. During experiments, the angular velocity of the wheel was held constant (17 deg/s), while longitudinal velocity was varied, for each slip level, according to the following equation:

$$i = 1 - \frac{v}{\omega r} \tag{5}$$

where v is the wheel longitudinal velocity, r is wheel radius, and ω is wheel angular velocity.

Note that the same definition of slip was used for positive and negative slip tests. Each test was repeated at least 15 times, and the data presented here was obtained as the average of all the trials.

Images for PIV analysis were collected while running the wheel flush against the 2.54 cm thick glass wall. For these experiments, a wheel was used with the exact same dimension but without a slot opening for the force sensors.

The ability to measure normal and tangential forces at the wheel-terrain interface, and the soil kinematics under the wheel, presents an opportunity to investigate the validity of the WR model when applied to lightweight vehicles.

This model is, in fact, based on the estimation of stress profiles along the wheel contact patch, and therefore it is intimately dependent on the ability to properly predict normal and tangential stresses along the wheel-terrain interface. A detailed description of the model is given in APPENDIX A; here only the equations relevant to this analysis will be discussed.

This section is organized as follows. A qualitative overview of measured stress data is presented first. Then, the force sensor reading is compared to that from an ATI force sensor and Futek torque sensor; this allows us to understand if the WR approach (i.e., calculate stress profiles and derive drawbar, torque, and sinkage from there) is valid for lightweight vehicles. Next, it is shown how the model parameters c_1 and c_2 are calculated from stress measurements. Finally, an analysis of the shear modulus k_x is performed and a modified WR model is presented.

3.1. Wheel-Terrain Interfacial Stress

Stress readings collected at various vertical loads were observed to follow similar trends, and therefore only data for F_z = 100 N is presented in Figure 3. These data illustrate how normal and tangential stress distributions vary along wheel width under low normal load. For low slip, the variation is minimal, while for high slip, stresses at the wheel edges (for high positive slip) or at the middle (for high negative slip) increase. Results for F_z = 100 N are summarized in Table 4 where the peak normal stress for each slip level is reported.

We hypothesize that stress variation at high slip is caused by the soil flow transport under the wheel: for high positive slip, the wheel displaces soil preferentially along the median axis. This is because the soil at either wheel edge remains stationary, and therefore material is preferentially transported through the middle. (The hypothesized soil motion profile is qualitatively similar to the fluid velocity profile present in open channel flow, where fluid velocity has a peak value at the channel centerline and zero velocity at the channel edges). As a result, the wheel load is preferentially supported by the wheel edges, where relatively less soil is displaced.

For negative slip, wheel motion tends to bulldoze material at the wheel's fore. For the same reasons expressed for the high positive slip case, material is transported preferentially along the centerline, where it tends to accumulate. As a result, the wheel travels on top of this small mass of material which, being at higher elevation along the centerline, increases stress along the wheel median axis.

It should be noted that Krick [9] reports opposite behavior for positive slip (negative slip is not tested): stress at the wheel edges decreases for high slip.

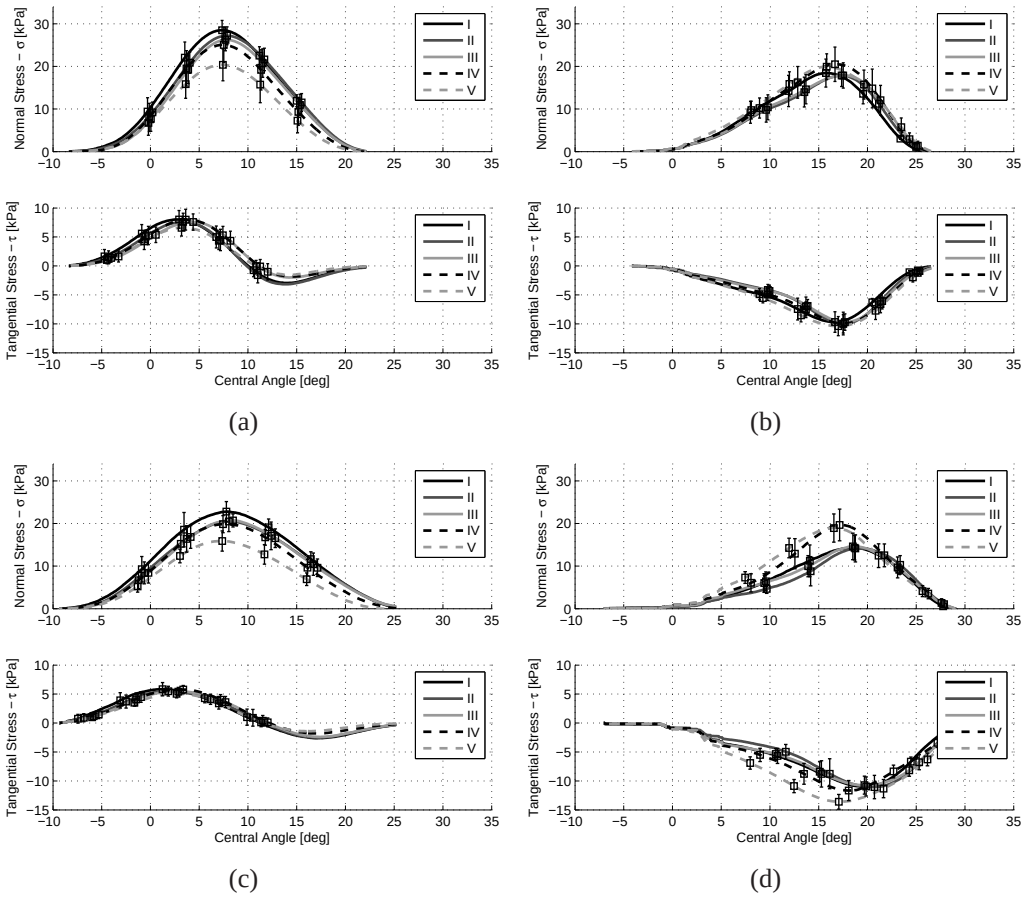

Figure 3: Normal and tangential stress for Fz = 100 N. (a) -30% slip. (b) +30% slip. (c) -70% slip. (d) +70% slip. These plots were obtained by averaging over all the tests (15 repetitions were conducted for each slip and load level). The boxplot represents the standard deviation for the data point.

Table 4: Peak normal stress for F_z = 100 N. Readings from sensors II, III, IV, and V are shown in absolute value and as percent variation with respect to sensor I. Large variations are observed for sensors IV and V at high slip.

i	σ_{max}^{I}	σ_{max}^{II}		σ_{max}^{III}		σ_{max}^{IV}		σ_{max}^{V}	
	[kPa]	[kPa]	[%]	[kPa]	[%]	[kPa]	[%]	[kPa]	[%]
-0.7	22.8	20.5	-10.1	20.7	-9.0	19.8	-12.9	15.9	-30.3
-0.5	24.6	23.1	-6.3	22.6	-8.1	21.1	-14.2	16.7	-32.3
-0.3	28.5	27.2	-4.6	26.2	-8.0	25.1	-12.1	20.4	-28.5
-0.1	27.3	26.5	-2.8	25.8	-5.4	26.3	-3.5	24.7	-9.6
0	26.4	27.1	2.7	24.7	-6.6	25.0	-5.4	25.3	-4.1
0.1	24.5	24.5	-0.2	23.4	-4.7	22.6	-7.8	19.8	-19.0
0.3	18.4	17.9	-3.1	17.9	-3.1	20.5	11.2	19.9	8.1
0.5	17.3	17.3	0.3	17.2	-0.4	19.7	13.9	19.0	10.3
0.7	14.3	14.2	-1.0	14.6	2.2	19.7	37.4	18.9	32.3

Excluding systematic experimental error, the reason could be explained by the different aspect ratio of the wheels: in this paper $w/r > 1$ while in [9] $w/r < 1$. (Unfortunately [9] does not report the wheel dimension; however, from photographic evidences it is clear that wheel width is smaller than wheel radius). Interestingly, Shamay [20], whose experiments are similar to [9], does not report higher stress at the edge of the wheel. On the contrary, in Shamay's experiments, the stress at the median axis of the wheel is always dominant. Hegedus [4] only measured normal stress at three locations (median axes and both wheel edges) and for positive slip and he noted that stress at the wheel median axis was always dominant. It should be mentioned that peak normal stress in the aforementioned studies was always above 50 kPa.

On the other hand, the wheel dimensions and loads used in Nagatani et al. [13] experiments are closer to the ones utilized in this work, and they suggest that normal pressure is dominant at the wheel median axis. However, it should be noted that in [13] only one slip level is presented, and shear stress is not measured at all. Moreover, a load button type load cell is used with only four sensing elements across the entire wheel width.

In experiments by Sela [17], Onafeko and Reece [15], and Oida et al. [14] the sensing device was not sensitive to stress variation across the wheel width, therefore it is not possible to draw any conclusion, from these studies.

3.2. Comparison of Stress Readings with Conventional Force/Torque Sensor

In order to evaluate the accuracy of the sensing array, and to verify the WR methodology, it is interesting to compare readings from the custom sensing array with ones derived from other sensors.

The ATI force-torque sensor continuously measures vertical load F_z and tractive force F_x acting on the wheel. (The load cell measures forces and torques in all directions, but only the aforementioned quantities are relevant to this analysis). Therefore it is possible to compare the readings obtained by the ATI load cell with the stress measurements from the sensing array as follows:

$$F_z^{ATI} \approx wr \int_{\theta_r}^{\theta_f} \tau^{SA} \sin\theta d\theta + wr \int_{\theta_r}^{\theta_f} \sigma^{SA} \cos\theta d\theta \tag{6}$$

$$F_x^{ATI} \approx wr \int_{\theta_r}^{\theta_f} \tau^{SA} \cos\theta d\theta - wr \int_{\theta_r}^{\theta_f} \sigma^{SA} \sin\theta d\theta \tag{7}$$

where F_z^{ATI} and F_x^{ATI} are the vertical load and drawbar force as measured by the ATI load cell, while τ^{SA} and σ^{SA} are the tangential and normal stress as measured by the custom sensing array. The angles θ_f and θ_r are derived from the sensing array readings, while w and r are respectively the wheel width and radius.

Similarly, the Futek torque sensor continuously measures the torque applied to the wheel by the motor. Thus, it is possible to compare the sensing array readings as follows:

$$M^{Futek} \approx wr^2 \int_{\theta_r}^{\theta_f} \tau^{SA} d\theta \tag{8}$$

where M^{Futek} is the torque applied to the wheel axle, as measured by the Futek torque sensor.

Although the test rig is equipped with a draw wire encoder that measures the vertical position of the wheel assembly, measurements from this sensor tend to be very sensitive to soil preparation (i.e., uneven terrain surface). For this reason sinkage was measured adopting a different methodology. Using a caliper, the depth of the rut left by the wheel was measured after each test was completed. The resulting wheel sinkage can be compared with the sensing array readings through the following equation:

$$z^{caliper} \approx r(1 - \cos\theta_f^{SA}) \tag{9}$$

where $z^{caliper}$ is the sinkage manually measured with the caliper and θ_f^{SA} is the entry angle derived from the sensing array readings.

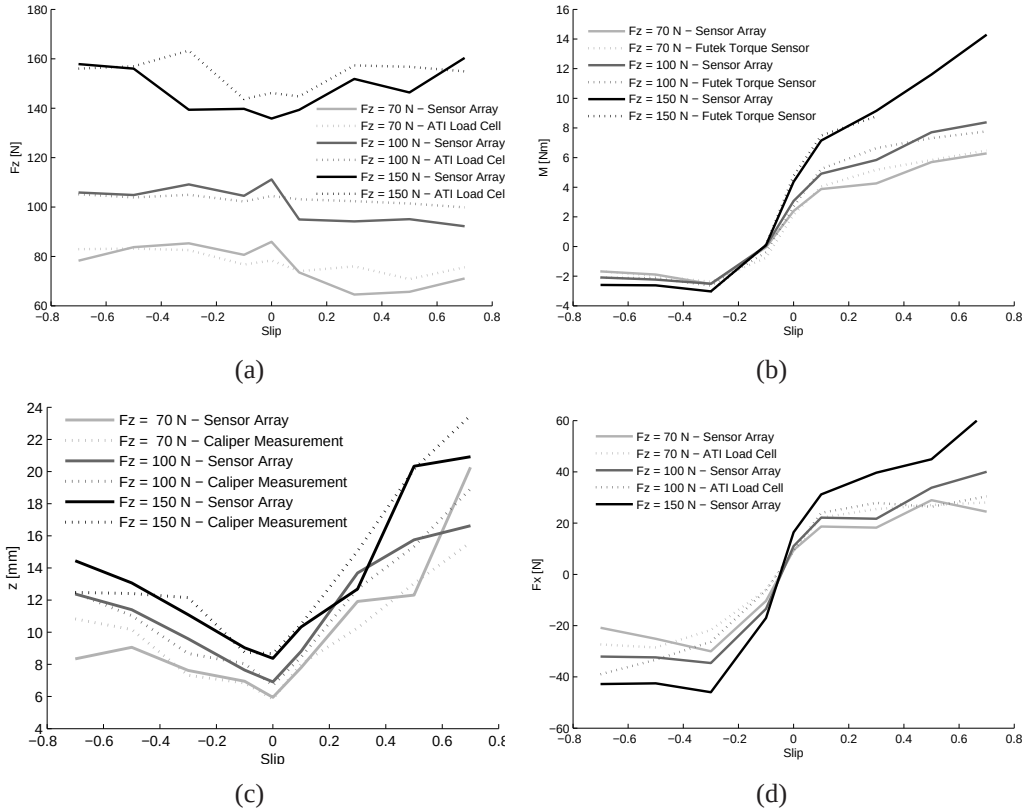

Figure 4: Readings from the custom sensing array are compared against readings obtained from the other sensors installed on the wheel. Comparison of (a) vertical load, (b) torque, (c) sinkage, and (d) tractive force are presented. Data is collected at 9 discrete points (see Table 5) but here is presented as continuous lines to improve visualization.

Data presented in Figure 4 show that the sensing array is in good agreement with data measured through other sources. Because of an unrecoverable sensor failure, drawbar pull data (i.e., F_x) for F_z = 150 N is not available. Torque reading was not available for F_z = 150 N and slip levels above 30% because of sensor saturation.

Table 5 shows the variation between the stress array readings and readings from the other instruments. Two error measures are presented: the absolute error Δ and the full scale percent error ε_f.

$$\Delta = X_{SA} - X_{other} \tag{10}$$

$$\varepsilon_f = \frac{\Delta}{X_f} \tag{11}$$

Table 5: Error between the sensing array readings and the other sensors mounted on the wheel. The full scale error ε_f shows that the sensing array readings and other sensors readings are in good agreement. The largest deviations are observed for drawbar force F_x readings.

F_z = 70 N

	F_z		F_x		M		z	
i	Δ [N]	ε_f [%]	Δ [N]	ε_f [%]	Δ [Nm]	ε_f [%]	Δ	ε_f [%]
-0.7	4.7	3.1	-6.5	-13.0	0.0	0.1	2.5	8.3
-0.5	-0.5	-0.4	-3.4	-6.8	-0.1	-0.6	1.1	3.7
-0.3	-2.8	-1.8	8.3	16.6	0.2	1.0	-0.3	-1.0
-0.1	-4.0	-2.6	4.3	8.7	-0.7	-4.7	-0.1	-0.4
0	-7.6	-5.0	-0.2	-0.4	-0.3	-1.7	-0.1	-0.3
0.1	0.5	0.3	3.5	7.0	0.2	1.1	0.2	0.7
0.3	11.4	7.6	7.3	14.5	0.9	6.1	-1.7	-5.5
0.5	5.2	3.4	-1.9	-3.8	0.1	0.9	0.7	2.4
0.7	4.5	3.0	3.6	7.2	0.2	1.3	-4.7	-15.6
AVG	**4.6**	**3.0**	**4.3**	**8.7**	**0.3**	**1.9**	**1.3**	**4.2**

F_z = 100 N

	F_z		F_x		M		z	
i	Δ [N]	ε_f [%]	Δ [N]	ε_f [%]	Δ [Nm]	ε_f [%]	Δ	ε_f [%]
-0.7	-0.7	-0.5	-6.9	-13.9	0.0	-0.1	0.1	0.2
-0.5	-1.0	-0.7	-1.0	-1.9	0.1	0.6	-0.4	-1.2
-0.3	-4.2	-2.8	8.3	16.6	-0.1	-0.9	-0.9	-3.0
-0.1	-2.3	-1.5	7.2	14.4	-0.4	-2.9	0.4	1.3
0	-6.7	-4.5	-1.8	-3.6	-0.4	-2.5	-0.2	-0.7
0.1	8.2	5.5	1.9	3.7	0.3	2.1	-0.3	-1.2
0.3	8.2	5.5	6.2	12.4	0.8	5.3	-1.0	-3.3
0.5	6.3	4.2	-7.4	-14.9	-0.4	-2.7	-0.4	-1.4
0.7	7.6	5.1	-9.6	-19.2	-0.6	-4.1	2.3	7.6
AVG	**5.0**	**3.3**	**5.6**	**11.2**	**0.4**	**2.3**	**0.7**	**2.2**

F_z = 150 N

	F_z		F_x		M		z	
i	Δ [N]	ε_f [%]	Δ [N]	ε_f [%]	Δ [Nm]	ε_f [%]	Δ	ε_f [%]
-0.7	-1.9	-1.2	n/a	n/a	n/a	n/a	-2.0	-6.6
-0.5	1.0	0.6	n/a	n/a	n/a	n/a	-0.7	-2.2
-0.3	24.0	16.0	n/a	n/a	0.0	-0.1	1.1	3.5
-0.1	4.0	2.7	n/a	n/a	0.0	0.1	-0.3	-0.9
0	10.4	6.9	n/a	n/a	0.4	2.7	0.3	1.0
0.1	5.5	3.6	n/a	n/a	0.3	2.3	0.2	0.5
0.3	5.5	3.7	n/a	n/a	-0.4	-2.5	2.4	7.9
0.5	10.4	6.9	n/a	n/a	n/a	n/a	-0.2	-0.6
0.7	-5.4	-3.6	n/a	n/a	n/a	n/a	2.6	8.6
AVG	**7.5**	**5.0**	**n/a**	**n/a**	**0.2**	**1.5**	**1.1**	**3.5**

where X_{SA} is the measure (either vertical load F_z, traction F_x, torque M, or sinkage z) obtained through the custom sensing array, X_{other} is the same quantity obtained with the ATI, Futek, or caliper sensor, and X_f is the full scale value for the quantity under investigation. The full scale values were selected assuming maximum, realistic, operation conditions: F_z = 150 N, F_x = 50 N, M = 15 Nm, z = 30 mm.

Overall, F_x is the measure that differs most on average, while more than half of the data points are below 5% full scale percent error ε_f.

3.3. Calculation of Coefficients for Determining the Relative Position of Maximum Radial Stress

The WR model [23, 24] depends on 6 terrain parameters (see Table 1) and three coefficients (θ_r, c_1, c_2). While the exit angle is usually approximated within the range of -10 to 0 degrees, there is virtually no knowledge of how the coefficients c_1 and c_2 can be estimated. The WR model in fact predicts that the normal stress will reach a maximal value for an angle θ_m that can be calculated as:

$$\theta_m = (c_1 + c_2 i)\theta_f \tag{12}$$

This linear relationship was introduced by Wong and Reece [23, 24] based on the observations of Onafeko and Reece [15]. Unfortunately, to date its accuracy has not been verified for lightweight vehicles. Also, it is not known if these parameters are independent of wheel vertical load. The custom sensing array enables us to investigate this matter further, since we can directly measure the angular location of maximum normal stress.

Figure 5(a) presents $(\theta_f, \theta_m, \theta_r)$ as functions of slip, for all tested load levels. In general, θ_m grows approximately linearly as positive slip increases. On the other hand, for negative slip, θ_m stays relatively constant.

Table 6: Coefficients for determining the relative position of maximum normal stress. The table includes the values calculated by this study (second and third column) together with the data available in the literature. Oida et al. [14] presented a set of coefficients, however these are omitted here because they were obtained with a flexible tire.

Coefficient	Positive Slip MIT	Negative Slip MIT	Positive Slip Onafeko I [23]	Positive Slip Onafeko II [23]	Positive Slip Hegedus [23]	Positive Slip Sela [23]
c_1	0.38	0.35	0.43	0.18	0.285	0.38
c_2	0.44	0.11	0.32	0.32	0.32	0.41

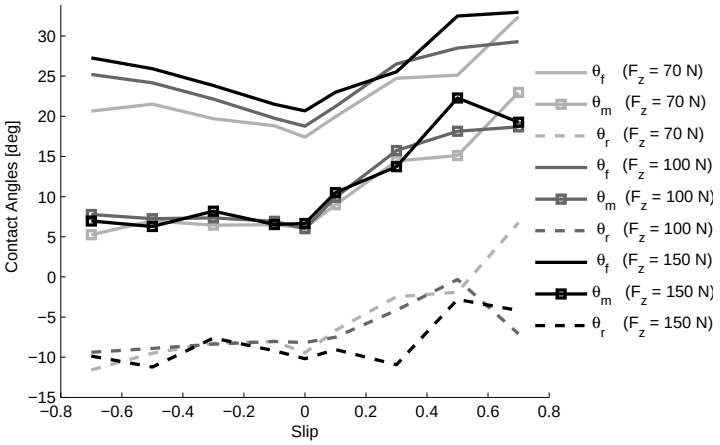

(a)

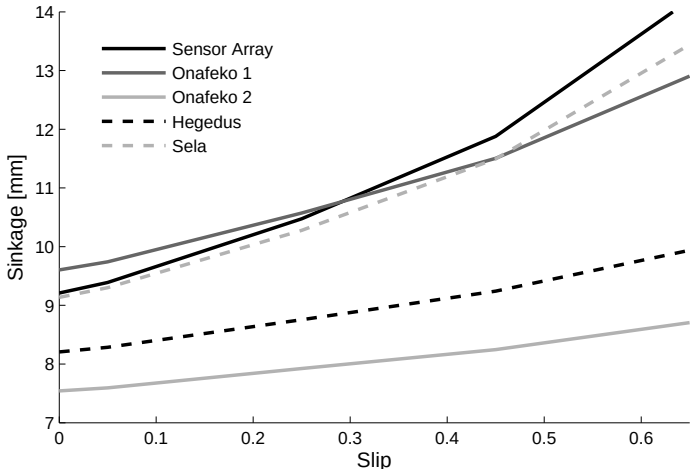

(b)

Figure 5: (a) Contact angles for F_z = 70 N, F_z = 100 N, F_z = 150 N, as function of wheel slip. (b) Slip sinkage characteristics obtained using Wong and Reece model and parameters presented in Table 6. This shows how coefficients c_1 and c_2 influence slip-sinkage behavior.

Another interesting observation is that the exit angle, θ_r follows a similar trend: it stays approximately constant for negative slip ratios and grows for positive slip ratios.

Constants c_1 and c_2, for both positive and negative slip, were obtained by linear regression and are presented in Table 6, together with the data available in the literature. Since it is believed that coefficients depend on wheel-terrain configuration, it is difficult to directly compare data because wheel size and terrain type utilized in this work is different from [4, 17, 15].

Nonetheless, it should be noted that c_1 and c_2 control slip-sinkage behavior, and therefore, when they are not explicitly available, they can be used as tuning parameters in order to obtain desired slip-sinkage characteristics. Ding et al. [3] suggested modification of the sinkage exponent n to improve slip-sinkage model response. However, it is usually not possible to directly measure the coefficients c_1 and c_2 (as opposed to the sinkage exponent, which can be evaluated with a plate penetration test) and therefore it is advisable to treat c_1 and c_2 as tuning parameters, rather than the sinkage exponent. The influence of c_1 and c_2 on slip-sinkage behavior is presented in Figure 5(b) where sinkage prediction for the parameters presented in Table 6 are presented (the curves are obtained using the WR model, F_z = 100 N, and soil parameters from Table 2).

3.4. Shear Displacement Calculation

Another critical aspect of the WR model is the calculation of soil shear displacement under the wheel. It is beneficial, at this point, to define three quantities that will be discussed in this section:

- The *theoretical tangential rim velocity* is defined as:

$$v_{rim} = r\omega - r\omega(1-i)cos\theta \tag{13}$$

  where r is wheel radius, ω is wheel angular speed, i is slip, and θ is the angular coordinate centered at the wheel axis (please refer to Figure 11). This is the tangential velocity of a point on the rim (located at angular position θ). It a scalar quantity and its definition is derived from kinematics.

- The *measured terrain tangential velocity* at the interface. This is the velocity of the soil adjacent to the wheel rim in the direction tangential to the wheel. It is obtained through PIV analysis, and is therefore a measured quantity labeled v_{piv}. Being the velocity tangent to the wheel rim, this is a scalar quantity.

- The *soil tangential slip velocity*, v_t, which represents the differential velocity between the wheel rim and the soil along the rim tangential direction. For measured data, v_t can be calculated as follows:

$$v_t = v_{rim} - v_{piv} \tag{14}$$

Wong and Reece postulated that soil shearing occurs at the wheel-terrain interface, and that the soil slip velocity is equal to the rim tangential velocity (for positive slip). Therefore, they proposed the following definition for the soil tangential slip velocity:

$$v_t = \begin{cases} r\omega - r\omega(1-i)cos\theta + K_v r\omega(1-i) & [\theta_m < \theta < \theta_f, i < 0] \\ r\omega - r\omega(1-i)cos\theta & [\theta_r < \theta < \theta_m, i < 0] \\ r\omega - r\omega(1-i)cos\theta & [\theta_r < \theta < \theta_f, i > 0] \end{cases} \tag{15}$$

As highlighted in the Wheel-Terrain Interfacial Stress section, the tangential stress goes through a sign inversion for negative slip. This was explained by Wong and Reece [24] as a result of bulldozed soil in front of the skidding wheel. The idea is that soil flows upward in front of the skidding wheel, creating an inversion of stress. Hence, they modified the slip velocity for negative slip by introducing a correction term K_v.

Visual inspection of the soil kinematics under a rigid wheel, however, has shown that soil at the wheel interface typically remains "attached" to the wheel rim, and there is little or no relative motion between the soil and the wheel rim. As a corollary to this, shearing does not occur at the wheel-terrain interface, but rather occurs along a failure plane internal to the soil.

Figure 6 shows the theoretical rim velocity together with the measured soil velocity at the rim (these are vectorial quantities, not to be confused with the tangential soil velocity which is only the component tangent to the wheel rim). The data clearly show that although the soil remains attached to the wheel, the measured velocity deviates from the theoretical rim velocity at the entry and exit angle where velocity gradients increase.

Using PIV techniques, it is possible to quantify, through equation 14, the slip velocity between the wheel rim and the soil in its proximity. Figure 7 presents results for -30% (a) and +30% (b) slip. The soil slip velocity is compared with predictions from the WR model (equation 15). For negative slip, the WR model is able to capture the velocity trend (see Figure 7(a)). The discontinuity in the model is due to the fact that the slip velocity is defined as a piecewise equation.

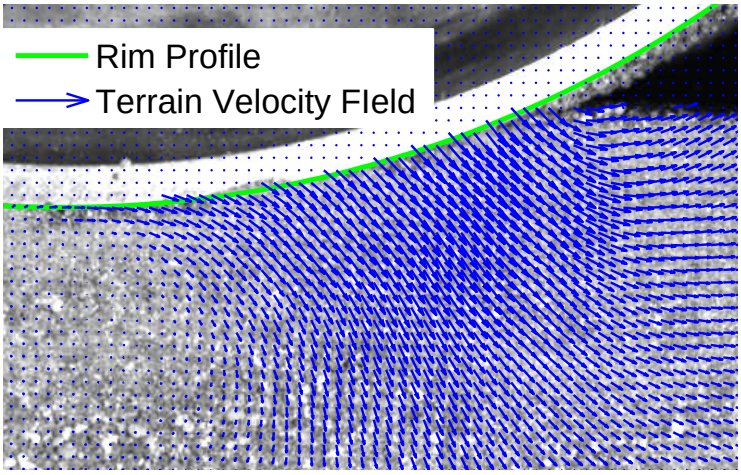

(a)

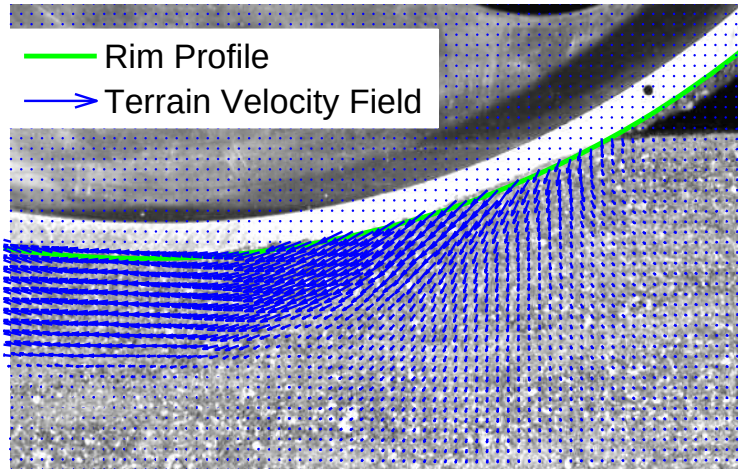

(b)

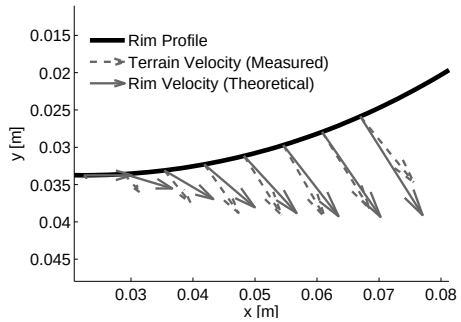

(c)

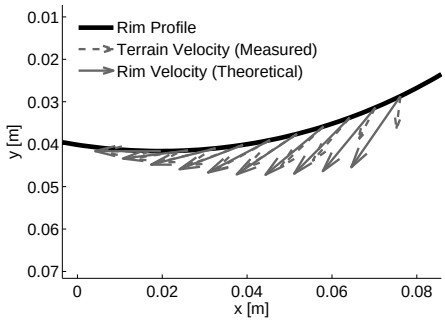

(d)

Figure 6: Soil velocity field for a -30% skidding wheel (a) and for a +30% slipping wheel (b). Soil behavior is markedly different for positive and negative slip. Soil velocity at wheel-soil interface is presented in figures (c) and (d).

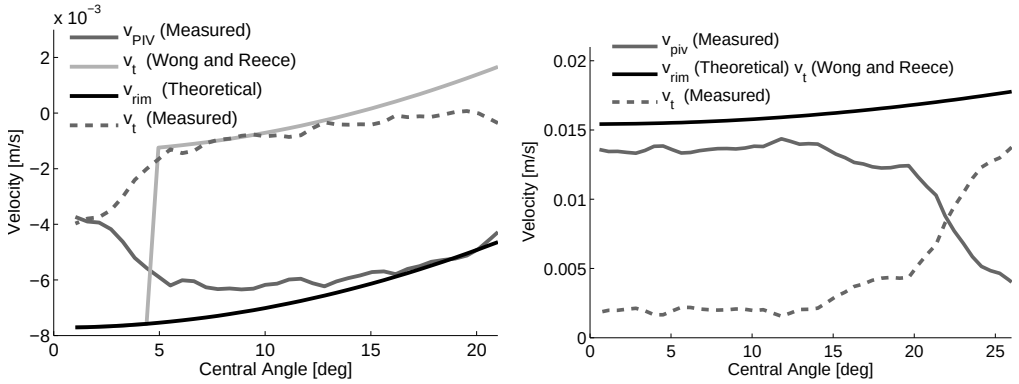

(a) (b)

Figure 7: Visualization of tangential slip velocities for -30% (a) and +30% (b) slip. v_{piv} is the terrain tangential velocity at the interface obtained through PIV measurements. v_t (Wong and Reece) is obtained through Equation 15. v_{rim} is the theoretical tangential rim velocity presented in Equation 13 and v_t measured is the soil tangential slip velocity calculated through Equation 14. Please note that v_t (Wong and Reece) and v_{rim} coincide for positive slip.

On the other hand, for positive slip (Figure 7(b)), the measured slip velocity is not close to the slip velocity predicted by WR model. (For positive slip, Wong and Reece postulated that the slip velocity corresponds to the rim velocity). This suggests that the slip velocity as proposed by Wong and Reece grossly overestimate the true soil slip velocity for positive slip.

However, it should be noted that the soil does not shear along a thin shearing plane. In fact, a large body of soil in proximity of the rim (an area of approximately 10 cm x 10 cm in our experiments) is influenced by wheel passage. For positive slip, periodic formations of shearing bands are observed (approximately 2 cm away from the wheel, as visible in Figure 6(b))[**? ? ?**], while for negative slip it is not possible to identify clear shearing bands. This suggests that the Wong and Reece approach to shear stress modeling represents only a coarse approximation to the complex state of stress and strain under the wheel. Further investigation into soil failure mechanisms for different slip levels is necessary to completely understand how to model shear stress under running gears.

3.5. Terrain Shear Modulus and Shear Stress Modeling

In the WR model, the shear stress is described as a function of the slip velocity:

$$\tau = (c + \sigma tan\phi)\left(1 - e^{-\frac{j}{k_x}}\right) \tag{16}$$

$$j = \int v_t d\theta \tag{17}$$

where c is the soil cohesion, σ is the normal stress, ϕ is the angle of internal friction, j is the shear displacement, and k_x is the soil shear modulus.

This formulation is based on two hypotheses:

H1 The soil slip velocity corresponds to the wheel rim velocity.

H2 The shear stress evolution at the interface is similar to the shear vs. displacement behavior observed during direct shear tests (or other types of shear tests).

The first hypothesis has already been discussed in section 3.4, while the second hypothesis will be investigated here.

Equation 16 was first introduced by Janosi and Hanamoto [8], and was used to describe shear vs. displacement behavior of granular materials in a low density state. The equation includes three terrain parameters: cohesion c, angle of internal friction ϕ, and shear modulus k_x. Cohesion and angle of internal friction are well understood (and intrinsic) soil parameters, while the shear modulus requires further discussion.

As we have noted in [18], the true shear modulus k_x (as presented in Table 2) for dry sand is usually much smaller than what is regularly reported in the terramechanics literature. According to the WR model, all the shearing occurs within few millimeters from the wheel rim. Although it was shown that this is not the case in practice, this assumption will be held valid for the sake of discussing the WR model. Figure 7(b) suggests that the slip velocity for positive wheel slip is highly over estimated using the Wong and Reece approach. As a result, Figure 8(b) shows how tangential stress, predicted by the WR model, is overestimated for positive slip. However, even for negative slip, where slip velocity is in good accordance with experimental evidence, if the measured shear modulus is utilized (see Table 2), the resulting shear stress is overestimated, as shown in Figure 8(a).

The analysis of the shear displacement and shear modulus suggests that both hypotheses H1 and H2 are not entirely true, and therefore the true shear modulus k_x is not representative of soil shearing behavior under the wheel. We note that shearing also depends on slip conditions, so k_x is unlikely to remain constant.

3.6. Model Adaptation

Thus far, the analysis has shown that although classical terramechanics models may not be able to precisely describe the fundamental phenomena at work,

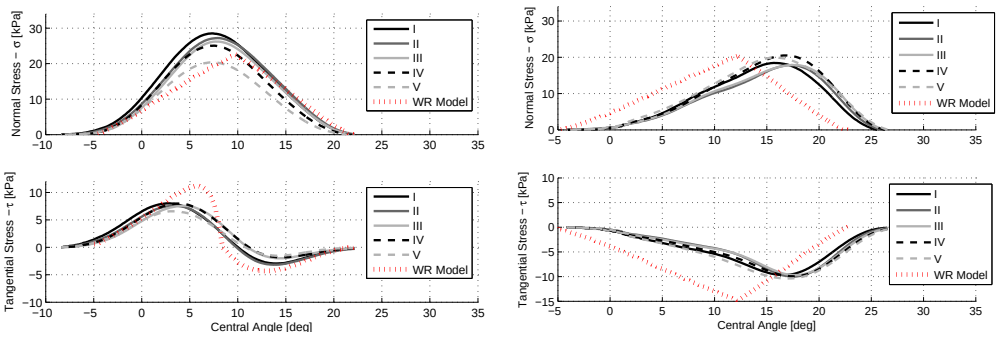

Figure 8: Comparison of Wong and Reece stress predictions with experimental data for -30% (a) and +30% (b) slip. These plots were obtained using a nominal k_x = 0.0006 and other soil parameters presented in Table 2. Tangential stress is overestimated for both positive and negative slip. This is because the nominal k_x. Note that for positive slip, there is a shift between WR model and measurements: this is because for that specific combination of slip and normal load, WR model is underestimating sinkage (i.e., entry angle is smaller). Exhaustive analysis of WR model behavior is presented in Figures 9, 10, and Table 7.

they are still able to describe all the salient characteristic of wheel terrain interaction. Unfortunately, these methods remain empirical in nature, and require some tuning in order to deliver satisfactory results. However, the analysis presented in this paper has led us to conclude that it is not necessary to introduce additional coefficients to produce reasonable model predictions.

Considering the results obtained from the analysis of shear displacement and shear modulus, we propose to retain the Wong and Reece shear displacement model untouched and modify the definition of shear modulus k_x. In fact, if the shear modulus k_x is made function of slip, it is possible to accurately model wheel behavior for a relatively large range of vertical loads, and for slip up to $\pm$70%. (We limit our analysis to $\pm$70% since our experimental data was collected within this range). We argue that the shear modulus should be viewed as an empirical parameter that governs the complex mapping between soil flow and shear stress at the wheel interface, and this study has shown that it cannot be simply extrapolated from direct shear tests and assumed a constant parameter value.

Figure 9 shows a comparison of torque M, traction F_x, and sinkage z between experimental data and the WR model. For the WR model, the parameters contained in Table 2 and Table 6 (the first two columns) have been used, with the

exception of k_x, which has been modified as follows:

$$k_x = c_x(i)k_{x0} \tag{18}$$

where c_x is a correction factor (a function of wheel slip) and k_{x0} is the nominal shear modulus (as presented in Table 2).

The correction factor was found by minimizing the following cost function:

$$f^2 = \left(wr^2 \int_{\theta_r}^{\theta_f} \tau d\theta - M^{SA} \right)^2 \tag{19}$$

where M^{SA} is the torque measured through the sensing array and the integral term is the torque as predicted by the Wong and Reece model (see APPENDIX A for details). Parameters for determining the correction factor c_x can be found in Table 8.

The piece-wise linear trend of the correction factor c_x can be explained in light of the failure mechanism under the wheel.

For large negative slip, braking force is primarily induced by normal stress, while shear stress has relatively less influence. In fact, Figure 3 shows that shear stress is approximately three times smaller for -70% slip as compared to +70% slip. Because of this, the shear modulus grows for negative slip, as presented in Figure 9(d). On the other hand, for small positive slip, the soil under the wheel does not develop full shearing bands, and therefore the shear modulus must be large in order to model the lack of traction produced. For increasing, positive slip, clearly discernible shear bands develop in the soil, and therefore the shear modulus again approaches its nominal value (i.e., the correction factor goes to one).

An alternative approach, aimed at simplifying the model, is to utilize the same shear velocity formulation for both positive and negative slip:

$$v_t = r\omega - r\omega(1-i)\cos\theta \tag{20}$$

As shown in Figure 7 this is not strictly correct, however, considering the empirical nature of this approach, it is not unreasonable. Note that this simplification only affects negative slip while the model remains unchanged for positive slip. The main benefit of this approach is that the model becomes continuous across the zero slip abscissa.

The simplified model is compared to experimental data in Figure 10. Prediction of torque, drawbar force, and sinkage with the simplified shear model is close to what was obtained with the original model (it is identical for positive

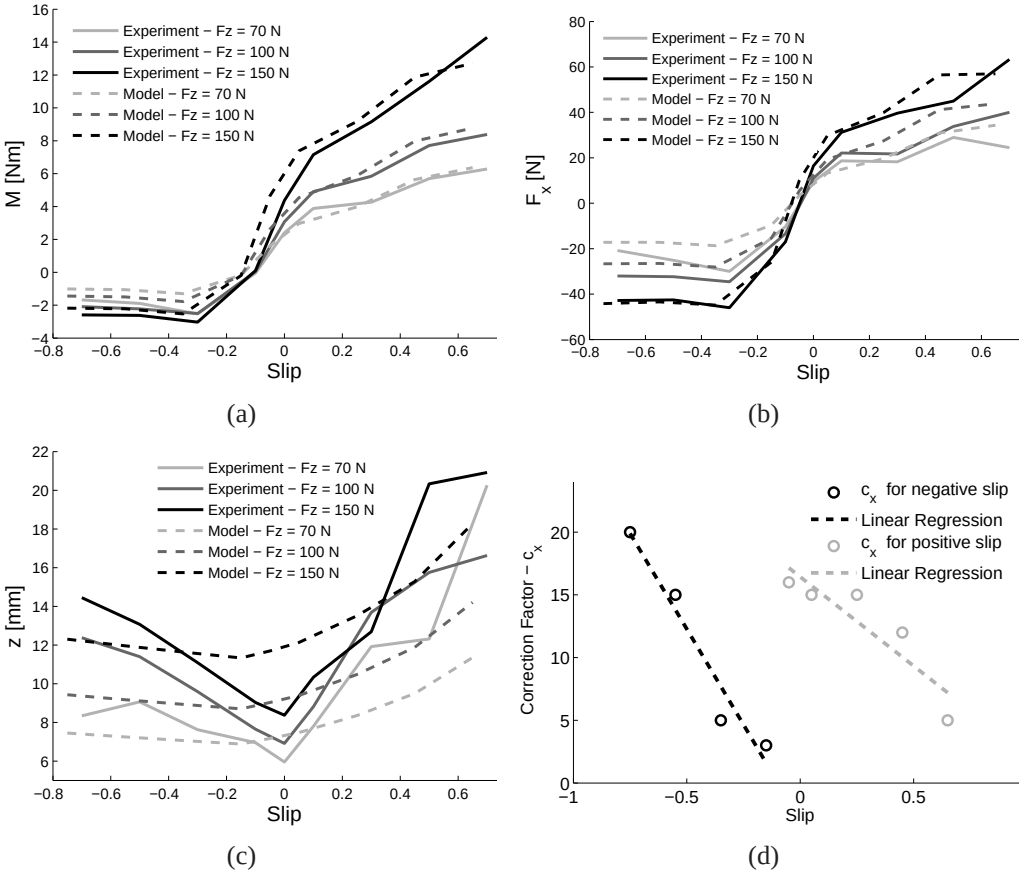

Figure 9: Comparison of Wong and Reece model with experimental data (sensing array) utilizing a correction factor (d) for the shear modulus k_x.

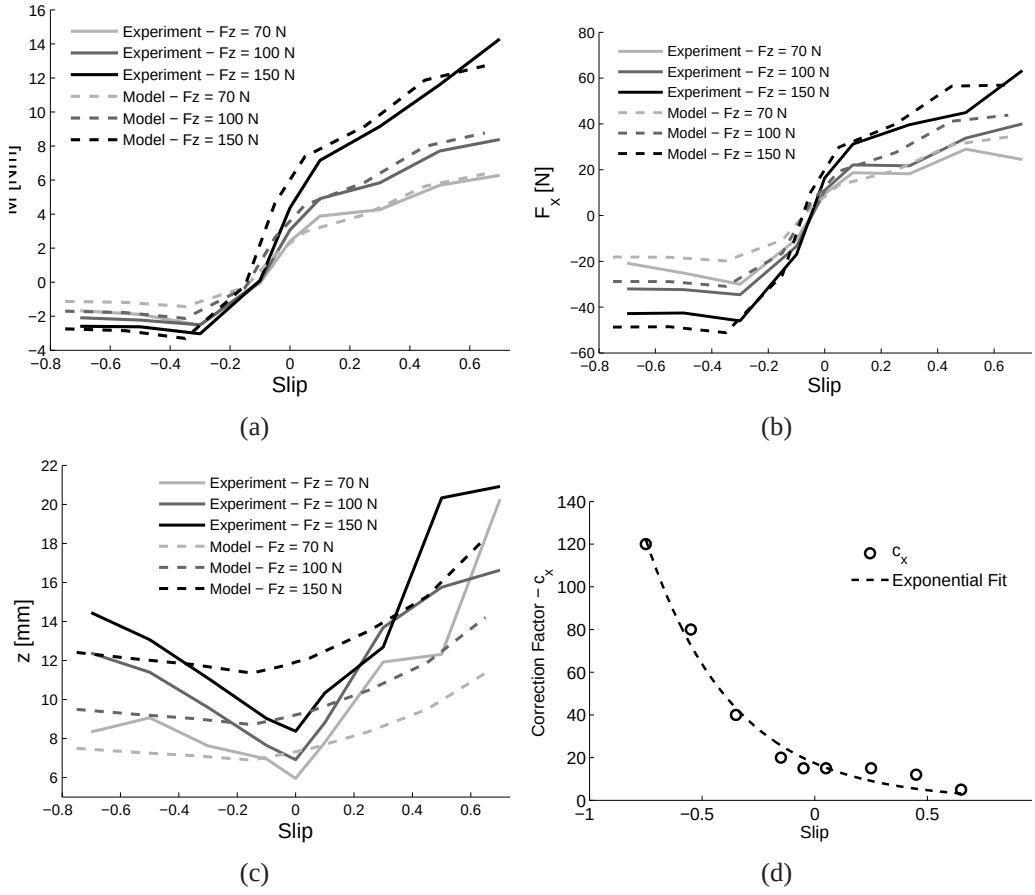

Figure 10: Comparison of the simplified model with experimental data utilizing a correction factor for the shear modulus k_x. The simplified model produces identical results to Wong and Reece model for positive slip and overall similar results for negative slip. The main advantage of the simplified model is to simplify the definition of shear displacement, avoiding discontinuity across zero slip.

Table 7: Absolute error Δ and full scale percent error ε_f of the WR model with respect to the sensing array readings. Average error stays below 11% with more than half of the data points below 5% error.

F_z = 70 N

	F_x		M		z	
i	Δ [N]	ε_f [%]	Δ [Nm]	ε_f [%]	Δ [mm]	ε_f [%]
-0.7	3.6	7.2	0.7	4.4	-0.9	-3.0
-0.5	7.9	15.8	0.8	5.5	-1.8	-6.0
-0.3	11.3	22.7	1.2	8.2	-0.6	-1.9
-0.1	0.7	1.4	-0.1	-0.8	-0.1	-0.2
0	-6.1	-12.2	-0.8	-5.3	1.2	4.1
0.1	-5.4	-10.7	-0.9	-6.1	-0.3	-1.1
0.3	1.4	2.9	-0.3	-1.9	-3.6	-11.9
0.5	1.9	3.9	-0.1	-0.4	-2.8	-9.4
0.7	9.9	19.7	0.1	0.6	-8.9	-29.7
AVG	**5.4**	**10.7**	**0.6**	**3.7**	**2.2**	**7.5**

F_z = 100 N

	F_x		M		z	
i	Δ [N]	ε_f [%]	Δ [Nm]	ε_f [%]	Δ [mm]	ε_f [%]
-0.7	5.4	10.7	0.6	4.3	-3.0	-9.8
-0.5	5.9	11.8	0.7	4.9	-2.2	-7.4
-0.3	6.5	13.0	0.7	4.8	-0.7	-2.2
-0.1	-1.9	-3.8	-0.2	-1.6	1.0	3.5
0	-5.5	-11.0	-0.4	-3.0	2.1	7.1
0.1	-2.8	-5.6	-0.4	-2.5	0.6	1.9
0.3	5.8	11.5	0.0	0.2	-3.2	-10.7
0.5	7.4	14.7	0.3	1.8	-3.9	-12.9
0.7	3.8	7.5	0.4	2.6	-2.4	-8.1
AVG	**5.0**	**10.0**	**0.4**	**2.9**	**2.1**	**7.1**

F_z = 150 N

	F_x		M		z	
i	Δ [N]	ε_f [%]	Δ [Nm]	ε_f [%]	Δ [mm]	ε_f [%]
-0.7	-1.4	-2.7	0.4	2.7	-2.2	-7.2
-0.5	-0.9	-1.9	0.4	2.6	-1.1	-3.7
-0.3	1.1	2.3	0.5	3.3	0.5	1.8
-0.1	-8.9	-17.8	-0.3	-2.0	2.3	7.7
0	-6.3	-12.5	0.3	1.9	3.3	11.1
0.1	-1.4	-2.7	0.2	1.5	1.8	6.0
0.3	0.2	0.4	0.0	0.1	0.8	2.7
0.5	11.5	23.1	0.3	1.7	-5.1	-16.8
0.7	-6.3	-12.7	-1.6	-10.5	-2.6	-8.8
AVG	**4.2**	**8.5**	**0.4**	**2.9**	**2.2**	**7.3**

slip). It is interesting to note that the shear modulus correction factor assumes an exponential decay. The reasons behind this behavior are the same as those highlighted above for the original model. However, with the simplified model, the correction factor becomes continuous because the shear displacement equation is continuous. The highly nonlinear behavior of c_x for negative slip is caused by the fact that with the simplified model, the shear stress does not undergo a sign inversion. This causes the torque to grow larger for negative slip, and therefore it requires a larger c_x, while in the original model the integral of τ was internally reduced by the sign change.

As shown in Table 7, the model is, on average, accurate within 11%. For a balanced analysis it is important at examine the full scale error ε_f. Sinkage error, although large in a relative sense is typically on the order of 2-5 millimeters. This is unsurprising considering the practical difficulty of preparing a perfectly flat soil surface for testing. In practice, run-to-run variation on the order of several mm is impossible to avoid.

Table 8: Correction factor parameters for the Wong and Reece model and for the simplified model.

	Wong and Reece ($c_x = p_1 i + p_2$)		Simplified ($c_x = p_1 e^{p_2 i}$)
	$i < 0$	$i \geq 0$	-
p_1	-31	-14	20.4
p_2	-3	16	-2.9

4. Conclusions

This paper presented an analysis of the interaction phenomena governing lightly loaded rigid wheel performance on dry sand. The stress analysis highlighted that stress distribution across wheel width varies significantly only for large slip. For large positive slip, stress is higher at the wheel edges, while for large negative slip the opposite is true. Comparison with the Wong and Reece model showed that this model is in theory able to characterize the mobility performance of lightweight vehicles. However, the empirical nature of method should not be forgotten. It was found that the coefficients c_1 and c_2 do not depend on vertical load, and therefore can be considered constant for a specific wheel-soil configuration. The analysis of soil kinematics under the wheel showed that the hypotheses behind the shear stress formulation are not entirely valid: this explains why the shear modulus k_x, obtained from direct shear tests (or other shear tests), does not produce accurate results when used in the Wong and Reece model.

ACKNOWLEDGEMENTS

This study was supported by the U.S. Army Tank Automotive Research, Development and Engineering Center (TARDEC) and the Army Research Office (ARO) under award number W911NF-13-1-0063. The authors are grateful to Dr. James W. Bales, the assistant director of the Edgerton Center at MIT, to Markus Wulfmeier, for his key contribution in developing the particle image velocimetry experiment, to Thuan Doan for his help in conducting experiments, and to Meccanotecnica Riesi SRL for collaborating on manufacturing the custom sensing array.

REFERENCES

[1] Beegle, L. W., Peters, G. H., Mungas, G. S., Bearman, G. H., Smith, J. A., Anderson, R. C., 2007. Mojave Martian Simulant: A New Martian Soil Simulant. In: Lunar and Planetary Institute Science Conference Abstracts.

[2] Bekker, M. G., 1969. Introduction to Terrain-Vehicle Systems. The University of Michigan Press, Ann Arbor.

[3] Ding, L., Gao, H.-b., Deng, Z.-q., Tao, J.-g., 2010. Wheel slip-sinkage and its prediction model of lunar rover. Journal of Central South University of Technology 17 (1), 129–135. URL http://dx.doi.org/10.1007/s11771-010-0021-7

[4] Hegedus, E., June 1963. Pressure distribution and slip-sinkage relationship under driven rigid wheels. Tech. rep., Army Tank-Automotive Center, Warren, MI Land Locomotion Laboratory.

[5] Iagnemma, K., Shibly, H., Dubowsky, S., 2005. A laboratory single wheel testbed for studying planetary rover wheel-terrain interaction. MIT Field and Space Robotics Laboratory Technical Report 1, 05–05.

[6] III, W. D. C., 1994. Trafficability of lunar microrovers (part 1). Tech. Rep. LGI TR94-02, Lunar Geotechnical Institute, Lakeland, FL.

[7] Ishigami, G., Miwa, A., Nagatani, K., Yoshida, K., 2007. Terramechanics-based for steering maneuver of planetary exploration rovers on loose soil. Journal of Field Robotics 24 (3), 233–250.

[8] Janosi, Z., Hanamoto, B., 1961. Analytical determination of drawbar pull as a function of slip for tracked vehicles in deformable soils. In: Proceedings of the 1st International Conference on Terrain-Vehicle Systems. Turin, Italy.

[9] Krick, G., 1969. Radial and shear stress distribution beneath rigid wheels and pneumatic tyres on yielding soils with regard to tyre deformation. Journal of Terramechanics 6 (3), 73 – 98.
URL http://www.sciencedirect.com/science/article/pii/0022489869901293

[10] Meirion-Griffith, G., Spenko, M., 2012. A pressure-sinkage model for small-diameter wheels on compactive, deformable terrain. Journal of Terramechanics (0), –.
URL http://www.sciencedirect.com/science/article/pii/S0022489812000274

[11] Moreland, S., Skonieczny, K., Wettergreen, D., Creager, C., Asnani, V., 2011. Soil motion analysis system for examining wheel-soil shearing. In: 17th International Conference for the Society of Terrain-Vehicle Systems.

[12] Murthy, T. G., Gnanamanickam, E. P., Saldana, C., Chandrasekar, S., 2009. Deformation field in indentation of granular materials. AIP Conference Proceedings 1145 (1), 263–266. URL http://link.aip.org/link/?APC/1145/263/1

[13] Nagatani, K., Ikeda, A., Sato, K., Yoshida, K., 2009. Accurate estimation of drawbar pull of wheeled mobile robots traversing sandy terrain using built-in force sensor array wheel. In: Intelligent Robots and Systems, 2009. IROS 2009. IEEE/RSJ International Conference on. pp. 2373–2378.

[14] Oida, A., Satoh, A., Itoh, H., Triratanasirichai, K., 1991. Three-dimensional stress distributions on a tire-sand contact surface. Journal of Terramechanics 28 (4), 319 – 330. URL http://www.sciencedirect.com/science/article/pii/002248989190013V

[15] Onafeko, O., Reece, A., 1967. Soil stresses and deformations beneath rigid wheels. Journal of Terramechanics 4 (1), 59 – 80. URL http://www.sciencedirect.com/science/article/pii/0022489867901048

[16] Richter, L., Ellery, A., Gao, Y., Michaud, S., Schmitz, N., Weiß, S., October 3-6 2006. A predictive wheel-soil interaction model for planetary rovers validated in testbeds and against mer mars rover performance data. In: Proceedings of 10th European Regional Conference of the ISTVS. Budapest, Hungary.

[17] Sela, A. D., June 1964. The shear to normal stress relationship between a rigid wheel and dry sand. Tech. rep., Army Tank-Automotive Center, Warren, MI.

[18] Senatore, C., Iagnemma, K., 2011. Direct shear behaviour of dry, granular soils subject to low normal stresses. In: Proceedings of 17th International Conference of the ISTVS. Blacksburg, VA.

[19] Senatore, C., Wulfmeier, M., MacLennan, J., Jayakumar, P., Iagnemma, K., 2012. Investigation of stress and failure in granular soils for lightweight robotic vehicle applications. In: Proceedings of NDIA Ground Vehicle Systems Engineering and Technology Symposium Modeling & Simulation, Testing and Validation (MSTV) Mini-Symposium. Troy, MI.

[20] Shamay, S. E., September 1971. Normal and shear stress distribution under a rigid wheel in dry sand. Tech. rep., Stevens Institute of Technology, Hoboken, NJ, Davidson Laboratory.

[21] Winter, A., 2011. Biologically inspired mechanisms for burrowing in undersea substrates. Ph.D. thesis, Massachusetts Institute of Technology.

[22] Wong, J., 1967. Behaviour of soil beneath rigid wheels. Journal of Agricultural Engineering Research 12 (4), 257–269.

[23] Wong, J. Y., Reece, A. R., 1967. Prediction of rigid wheel performance based on analysis of soil-wheel stresses, Part I. Performance of driven rigid wheels. Journal of Terramechanics 4 (1), 81–98.

[24] Wong, J. Y., Reece, A. R., 1967. Prediction of rigid wheel performance based on analysis of soil-wheel stresses, Part II. Performance of towed rigid wheels. Journal of Terramechanics 4 (2), 7–25.

APPENDIX A

The Bekker-Wong-Reece model relies on analysis of two fundamental relationships: the pressure-sinkage relationship, and the shear stress-shear deformation relationship. In the context of rover mobility, the pressure-sinkage relationship governs the depth that a rover wheel will sink into the terrain and therefore

how much resistance it will face during driving. The shear stress-shear displacement relationship governs the amount of traction that a wheel will generate when driven and therefore how easily it will progress through terrain and surmount obstacles. The pressure-sinkage relationship was described by Bekker in the form of a semi-empirical equation that relates sinkage with normal pressure of a plate pushed down into the soil. The proposed relation is commonly referred as the Bekker equation, and provides a link between the kinematics (sinkage) and stress (pressure) of a plate (which can be viewed as a proxy for a wheel or track):

$$p = \left(\frac{k_c}{b} + k_\phi \right) z^n \tag{21}$$

Parameters k_c, k_ϕ, n are empirical constants that are dependent on soil properties, while b corresponds to the plate width. These parameters can be obtained from field tests conducted with a device called a bevameter. Specifically, stress can be divided in two components (assuming a two dimensional model, and momentarily ignoring out of plane motion): normal stress and tangential stress. A schematic representation of the stress distribution at a wheel-terrain interface is presented in Figure 11. Normal stress can be calculated by starting with Bekker's pressure-sinkage relation, and introducing a scaling function intended to satisfy the zero-stress boundary conditions present at the fore and aft points of contact of the wheel with the terrain (known as "soil entry" and "soil exit"). The equation is expressed as a piece-wise function, as follows:

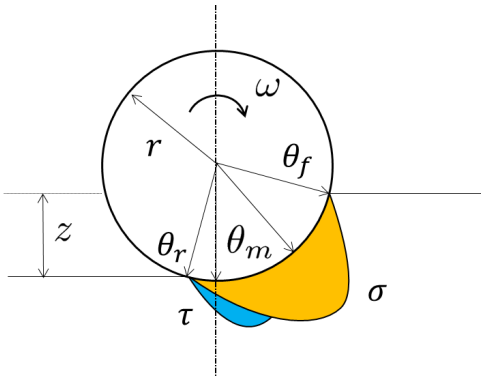

Figure 11: Schematic representation of normal and tangetial stress profile along a the wheel-soil interface.

$$\begin{aligned}
\sigma &= \begin{cases} \sigma_1 = \left(\frac{k_c}{b} + k_\phi\right) z_1^n & \theta_m < \theta < \theta_f \\ \sigma_2 = \left(\frac{k_c}{b} + k_\phi\right) z_2^n & \theta_r < \theta < \theta_m \end{cases} \\
z_1 &= r(\cos\theta - \cos\theta_f) \\
z_2 &= r\left(\cos\left(\theta_f - \frac{\theta - \theta_r}{\theta_m - \theta_r}(\theta_f - \theta_m)\right) - \cos\theta_f\right)
\end{aligned} \tag{22}$$

where θ_f is the soil entry angle, θ_r is the exit angle, and θ_m is the angle at which the maximum normal stress occurs (see Figure 11). Wong and Reece suggested use of a linear equation to calculate θ_m:

$$\theta_m = (c_1 + c_2 i)\theta_f \tag{23}$$

The shear stress-shear displacement relationship is based on the Mohr-Coulomb failure criterion, coupled with a modulation function proposed by Janosi and Hanamoto [8]:

$$\tau = (c + \sigma tan\phi)\left(1 - e^{-\frac{j}{k_x}}\right) \tag{24}$$

where c is the soil cohesion, ϕ is the angle of internal friction, k_x is the shear modulus (a measure of shear stiffness), and j is shear deformation:

$$j = \int_0^{t_0} v_t d\theta = \int_\theta^{\theta_f} v_t \frac{d\theta}{\omega} \tag{25}$$

where v_t is the tangential slip velocity and k_x is the shear modulus. Expressing v_t as a function of angular velocity and slip, it is possible to obtain an expression for shear displacement in closed form for positive slip:

$$v_t = r\omega - r\omega(1-i)cos\theta \tag{26}$$

$$j^+ = r\left[\theta_f - \theta - (1-i)(\sin\theta_f - \sin\theta)\right] \tag{27}$$

For negative slip, starting from the observation that soil flows upward at the leading edge of the wheel, Wong and Reece proposed a modified equation for the slip velocity between θ_f and θ_m:

$$v_t = r\omega - r\omega(1-i)cos\theta + K_v r\omega(1-i) \quad \theta_m < \theta < \theta_f \tag{28}$$

The constant K_v was calculated by requiring that the shear displacement should be zero for $\theta = \theta_f = \theta_m$, leading to:

$$K_v = \frac{1}{(1-i)}\left[\frac{(1-i)(\sin\theta_f - \sin\theta_m)}{\theta_f - \theta_m} - 1\right] \tag{29}$$

It should be noted that Wong and Reece proposed a different approach for calculating θ_m for negative slip, while here we will assume that the same linear expression can be used. Also, Wong and Reece used positive values for skid; hence the sign of slip i is inverted here (slip is defined by Equation 5). Therefore, the shear displacement for negative slip can be written as:

$$j^- = \begin{cases} r[(\theta_f - \theta)(1 + K_v(1-i)) - (1-i)(\sin\theta_f - \sin\theta)] & \theta_m < \theta < \theta_f \\ r(\theta_m - \theta - (1-i)(\sin\theta_m - \sin\theta)) & \theta_r < \theta < \theta_m \end{cases} \tag{30}$$

This definition of shear displacement allows the Wong and Reece model to predict shear displacement sign inversion. Once the stress profile acting on a wheel has been completely defined, these profiles can be integrated to determine the net forces and torques, which are then summed to compute overall vehicle motion. Traction forces generated by a wheel can be decomposed in two components: a thrust component, which acts to move the vehicle forward; and a compaction resistance component, which resists forward motion. Thrust, T, is computed as the sum of all shear force components in the direction of forward motion:

$$T = wr\int_{\theta_r}^{\theta_f} \tau\cos\theta d\theta \tag{31}$$

Compaction resistance, R_c, is the result of all normal force components acting to resist forward motion, and can be thought of as the net resistance force provided by the soil:

$$R_c = wr\int_{\theta_r}^{\theta_f} \sigma\sin\theta d\theta \tag{32}$$

The net longitudinal force, also termed the drawbar pull, F_x , is calculated as the difference between the thrust force and resistance force. F_x is the resultant force that can provide a pulling/braking force at the vehicle axle.

$$F_x = T - R_c \tag{33}$$

The importance of drawbar force is obvious, since a positive drawbar force implies that a rover can generate forward motion on a particular patch of terrain,

while a negative drawbar force suggests that forward motion is difficult or impossible. Torque, M, is the resultant of shearing action along wheel rim, and can be calculated as:

$$M = wr^2 \int_{\theta_r}^{\theta_f} \tau d\theta \tag{34}$$

The sinkage of a wheel can be calculated by solving a vertical force equilibrium problem, which enforces the fact that the force resisting wheel penetration into the soil must be balanced by the vertical load acting on that wheel.

$$F_z = wr \int_{\theta_r}^{\theta_f} \tau \sin\theta d\theta + wr \int_{\theta_r}^{\theta_f} \sigma \cos\theta d\theta \tag{35}$$

Please note that the balance of vertical load is the first equation that must be solved in order to define entry and exit angles θ_f and θ_r (as previously noted, exit angle θ_r is usually held constant).